Carbon deposition in CH4/CO2 operated SOFC: Simulation and experimentation studies

K. Girona, J. Laurencin, J. Fouletier, F. Lefebvre-Joud

Carbon deposition in CH_4/CO_2 operated SOFC: Simulation and experimentation studies

K. Girona [a,*], J. Laurencin [b], J. Fouletier [c], F. Lefebvre-Joud [b]

[a] *IRCELYON UMR 5256 CNRS Université Claude Bernard Lyon 1, 69622 Villeurbanne Cedex, France*
[b] *LITEN/DTH/LEV CEA Grenoble, 17 rue des Martyrs, 38054 Grenoble Cedex 9, France*
[c] *LEPMI, UMR 5279, CNRS-Grenoble INP-Université de Savoie-Université Joseph Fourier, BP75, 38402 Saint Martin d'Hères Cedex, France*

Due to their high operating temperatures, SOFCs can be directly fed with biogas, mainly composed of CH_4 and CO_2. In this work, experiments was performed with a classical Ni-YSZ cermet//YSZ//LSM cell fed either with a synthetic simulated biogas (CH_4/CO_2 ratio equal to 1 with 6% humidity), or with humidified H_2. In both cases, the performances are found to be very similar, which confirms the ability of SOFCs to operate with internal reforming of biogas. Nevertheless, carbon formation in these operating conditions needs to be considered because of durability concerns. Thermodynamic calculations and modelling are carried out to evaluate the risk of carbon deposition depending on operating parameters. In the ternary diagram C H O, the limits for carbon deposition are plotted, allowing the determination of "safe" operating conditions in terms of CH_4 inlet flow rate and cell voltage. First experiments confirm these modelling results.

1. Introduction

The most attractive feature of Solid Oxide Fuel Cells is high fuel flexibility due to high operating temperatures (800–1000 °C). Using an external reformer, various fuels such as hydrocarbons are converted to H_2 and CO and H_2 + CO mixtures are then introduced into the anode system. Alternatively, the internal reforming process has been developed as a more advantageous concept for SOFCs. In this process, the reforming reactions occur within the anode. Various fuels such as natural gas, ethane, butane, toluene, gasoline and alcohols have been tested: the feasibility of this concept either on the classical cermet Ni-YSZ anode [1–4] or on various anode materials [5–10] has been demonstrated. Since methane is the main constituent of natural gas, numerous investigations on fuel cells operating under Direct Internal Reforming (DIR) of methane have been reported [11–18]. Although CH_4 reforming can be performed by steam as well as by CO_2, most of the DIR investigations have used steam as reforming agent, while only few studies concern fuel cells using CO_2 in the reforming process.

Renewed interest for CO_2 reforming also called "dry reforming" appeared recently, with the direct operation of SOFCs with biogas [4,19–22]. Produced by the fermentation of biomasses and agricultural wastes, this biogas is mainly composed of CH_4 (50–70%) and CO_2 (25–50%) with several minor components such as H_2 (1–5%) or N_2 (0.3–3%) and impurities like NH_3, H_2S or halides [23]. Due to the high proportion of CO_2 in biogas, H_2 and CO are mainly produced by the CO_2 reforming reaction achieved within the SOFC anode. As the use of biomass does not contribute to additional CO_2 emission, this concept could be a suitable way for energy production.

However, several major problems have to be solved before cells can operate continuously using hydrocarbons or biogas. The risk of carbon deposition on the anode surface at high operating temperatures and the presence of impurities in the fuels can dramatically reduce the performance and durability of the cells [1,24–26]. Moreover, the risk of cell degradation is very high with Ni-based anode since Ni is a good catalyst for both hydrocarbons reforming and carbon deposition reactions. Carbon deposition has been reported to occur on the active sites of the anode resulting in rapid and irreversible deactivation [17]. In order to limit the deactivation of the anode caused by carbon formation, several solutions are proposed.

The first approach is to use appropriate anode formulations that do not promote carbon formation. For example, addition of precious metals to the classical Ni-YSZ anode [27] or use of Scandia-Stabilized Zirconia (ScSZ) instead of YSZ in the Ni-based anode [6,7,11,28] have been reported to reduce carbon deposition. Substituting Cu or CeO_2 for Ni in the anode has been widely studied [5,8,10,12,25,26].

The second approach consists in using conventional Ni-YSZ cermet as anode with an excess of steam or CO_2 in the anodic fuel, so that carbon deposition is thermodynamically hampered. Experimental studies have demonstrated the feasibility of this concept [3,4,19,20,29,30]. However, an important quantity of H_2O in the system can induce damage on the cell (water management problem and Ni oxidation). Another strategy to prevent carbon formation in Ni-based anodes has also been studied, i.e., working at low temperature, below the threshold at which pyrolysis occurs. For example, at 700 °C and with a low anodic polarization, SOFCs are stable under methane without coking [18]. Minimizing the free volume within the Ni anode would also significantly decrease the amount of carbon by reducing the residence time of the fuel [1,29,31]. Carbon deposition is also influenced by the supply of oxide ions through the electrolyte driven by the external current. Studies have shown that cell polarization can reduce carbon deposition within the anode due to carbon oxidation [2,18,19,32–34].

Consequently, appropriate operating conditions have to be determined to avoid damage induced by carbon formation, whatever the anode material. To achieve stable DIR operations, thermodynamic analysis can be used in order to determine the conditions in which carbon is thermodynamically unstable. This preliminary study allows to predict the required fuel/H_2O, fuel/CO_2 ratios or the threshold current density value [1,3,4,16,17,35]. The purpose of this study is to evaluate the electrochemical performances of a classical Ni-YSZ cermet//YSZ//LSM planar cell fed with a synthetic biogas (CH_4/CO_2, ratio equal to 1, with 6% humidity). In parallel to the experimental study, electrochemical and thermal models of the DIR process were adapted to a single test rig. The simulations allow giving the fuel compositions in the anode and the cell temperature as functions of CH_4 inlet flow rate and cell voltage. According to these operating parameters, thermodynamic calculations have been carried out to evaluate the risk of carbon deposition. In the ternary diagram C—H—O, the limits for carbon deposition were plotted at different temperatures using a calculation code, defining "safe" operating conditions.

2. Experimental

2.1. Materials tested

A commercial circular anode supported cell[1] fed either with a synthetic biogas or with humidified H_2 was tested. The anode substrate was a double layer made of a dense nickel oxide layer (NiO) 8–10 μm thick, and a porous nickel-YSZ cermet (8 mol% Y_2O_3)

[1] FZJ SOFC, www.fz-juelich.de.

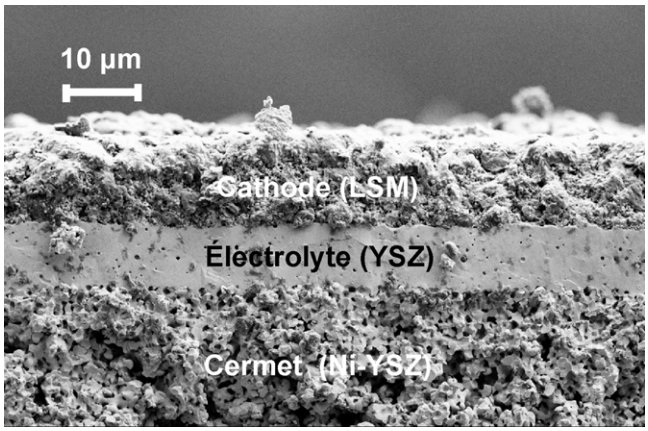

Fig. 1. SEM micrograph of a fractured cross section of the cell after test.

with a total thickness of about 1.5 mm. The electrolyte was a dense YSZ layer, 8–10 μm thick, the cathode was a Strontium-doped Lanthanum Manganite (LSM) layer. The cell diameter was 56 mm with an active area of 12.5 cm^2. Fig. 1 shows a SEM image of the fractured cross section of the cell after test.

2.2. Cell preparation and procedure

The cell was sealed between two ceramic (YSZ) holding rings. A glass paste deposited on the electrolyte layer made the sealing. The cell and its holding rings were placed between two alumina tubes. Two gold rings between the zirconia rings and the alumina tubes ensured gas tightness between the anode and the cathode sides. Fig. 2 shows the details of the single cell test and sealing system.

The glass seal was optimized by heat treatment at 900 °C during 1.5 h. Gold mesh (Au-mesh wires 0.25 mm in diameter and 64 meshes cm^{-2}) was used as current collector on the Ni-YSZ cermet anode (low activity of gold towards CH_4 reforming reactions) and on the LSM cathode. A compressive stress of 7500 Pa was applied on these current collectors in order to improve contact resistances.

Gaseous species were introduced at the anode and cathode peripheries and evacuated at the centre after chemical and electrochemical reactions. Four thermocouples were placed in the device to measure the temperatures of anode and cathode gases at both the inlet and the outlet gas channels.

After reducing NiO to Ni at 900 °C, electrochemical measurements in humidified H_2 and CH_4/CO_2 were performed at 800 °C. Table 1 gives the fuel compositions and flow rates tested at the anode side. The fuel composition A corresponds to the initial test under H_2 humidified at 3%. The fuel compositions B, C, D, E and F represent the tests under biogas humidified at 6% with the CH_4/CO_2 ratio kept constant to 1 (composition representative of synthetic simulated biogas produced from the processing of paper effluents). The total flow rate was maintained at 212 mL min^{-1} (15.8 mol s^{-1}). The cathode was exposed to air at a flow rate of 520 mL min^{-1} (38.9 mol s^{-1}).

3. Modelling

Two interconnected models were developed to simulate the behaviour of the cell on a single test rig. The first model describes the electrochemical behaviour of the cell. It is coupled to a second model that calculates the temperature field within the cell and the ceramic test system. The circular shape of this system allowed using an axisymmetric analysis (cf. Fig. 2).

3.1. Electrochemical model

The electrochemical model of the DIR process has been detailed by Morel et al. [36]. A mass balance on each species was calculated along the gas channel. Mass transport through the thick porous anode was described by the Stephan–Maxwell and Knudsen diffusion equations. It was assumed that the steam or CO_2 reforming reactions occur on the surface of the anode materials (Eq. (1) and Eq. (2)) whereas the Water Gas Shift reaction (WGS, Eq. (3)) occurs in the void fraction of the anode. This approach was previously described by Lehnert et al. [37]

$$\text{Steam reforming reaction} \quad CH_4 + H_2O \Leftrightarrow CO + 3H_2 \tag{1}$$

$$\text{reforming reaction} \quad CH_4 + CO_2 \Leftrightarrow 2CO + 2H_2 \quad CO_2 \tag{2}$$

$$\text{WGS reaction} \quad CO + H_2O \Leftrightarrow CO_2 + H_2 \tag{3}$$

Considering Ni as the catalytic phase, the kinetic constants for both steam and CO_2 reforming reactions were considered very close to each other [38].

Owing to the chosen operating conditions, the carbon deposition reactions were not considered in the present model.

In this model, only H_2 anodic oxidation was taken into account. The CO anodic oxidation was neglected because a large fraction of CO was supposed to be converted into CO_2 via the WGS reaction, which is assumed to be close to thermodynamic equilibrium. According to the data obtained from the electrochemical model, the value of the constant calculated from the partial pressures of H_2, CO_2, CO and H_2O present at the anode, under these operating conditions ($k = (P[H_2]P[CO_2])/(P[CO]P[H_2O])$, see Eq. (3)) was very close to the value of the equilibrium constant at 800 °C ($K_{eq} = 1$). The local current density was related to the H_2 production which occurred at the anode/electrolyte interface by the Faraday law (Eq. (4)).

$$N_{H_2} = \frac{i}{2F} \,(\text{mol s}^{-1}\,\text{m}^{-2}) \tag{4}$$

with N_{H_2} the H_2 flux density, i the local current density and F the Faraday constant.

The cell voltage U_{cell} was imposed and assumed to be constant over the cell active area. The local current density was calculated in order to verify the following equation across the cell:

$$U_{cell} = E_{i=0} - R_t i - (\eta_{conc,a} + \eta_{act,a} - \eta_{conc,c} - \eta_{act,c})(\text{V}) \tag{5}$$

where $E_{i=0}$ is the Open Circuit Voltage (OCV), R_t the cell resistance (including the electrolyte ohmic resistance and the contact resistance between current collectors and electrodes), η_{act} and η_{conc} respectively, the activation and the concentration overpotentials (a for anode and c for cathode).

The OCV (Eq. (6)) and the anode concentration overpotential (Eq. (7)) were written according to the Nernst equation:

$$E_{i=0} = \frac{-\Delta G_{H_2O}^{\circ}}{2F} + \frac{RT}{2F} \ln\left(\frac{P_{H_2}^{a,i=0}\left(P_{O_2}^{c,i=0}\right)^{1/2}}{P_{H_2O}^{a,i=0}}\right) (\text{V}) \tag{6}$$

$$\eta_{conc,a} = \frac{RT}{2F} \ln\left(\frac{P_{H_2O}^{a,i\neq 0} P_{H_2}^{a,i=0}}{P_{H_2}^{a,i\neq 0} P_{H_2O}^{a,i=0}}\right) (\text{V}) \tag{7}$$

A phenomenological law was used to determine the cathodic concentration overpotential by using a limiting current density. A high value was considered for the latter parameter and justified by the very thin cathode layer. The activation polarizations were calculated with the Butler–Volmer equation. Table 2 gives the chosen kinetic and electrochemical parameters values.

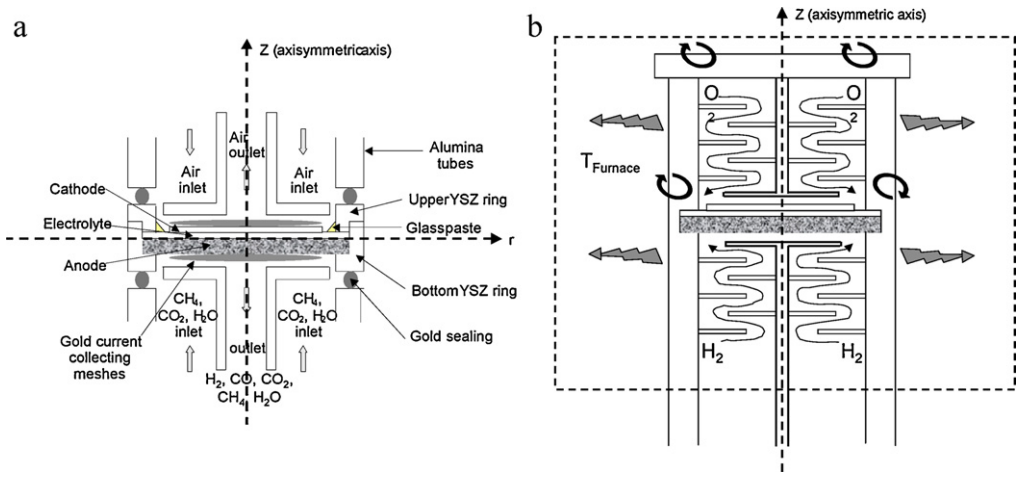

Fig. 2. Test device used for the electrochemical measurements. (a) Schematic diagram of the test cell and sealing system. (b) Schematic diagram of the ceramic test system.

Table 1
Flow rates and mole fractions of CH_4 (x_{CH_4}) at room temperature.

Fuel composition (x_{CH_4})	H_2 (mL min^{-1}/mol s^{-1})	CH_4 (mL min^{-1}/mol s^{-1})	CO_2 (mL min^{-1}/mol s^{-1})	Ar (mL min^{-1}/mol s^{-1})	H_2O (mL min^{-1}/mol s^{-1})
A ($x_{CH_4} = 0$)	$225/9.39 \times 10^{-5}$	0/0	0/0	0/0	$7/0.28 \times 10^{-5}$
B ($x_{CH_4} = 0.47$)	0/0	$100/7.45 \times 10^{-5}$	$100/7.45 \times 10^{-5}$	0/0	$12/0.89 \times 10^{-5}$
C ($x_{CH_4} = 0.24$)	0/0	$50/3.73 \times 10^{-5}$	$50/3.73 \times 10^{-5}$	$100/7.45 \times 10^{-5}$	$12/0.89 \times 10^{-5}$
D ($x_{CH_4} = 0.12$)	0/0	$25/1.86 \times 10^{-5}$	$25/1.86 \times 10^{-5}$	$150/11.18 \times 10^{-5}$	$12/0.89 \times 10^{-5}$
E ($x_{CH_4} = 0.06$)	0/0	$12/0.89 \times 10^{-5}$	$12/0.89 \times 10^{-5}$	$176/13.12 \times 10^{-5}$	$12/0.89 \times 10^{-5}$
F ($x_{CH_4} = 0.03$)	0/0	$6/0.45 \times 10^{-5}$	$6/0.45 \times 10^{-5}$	$188/14 \times 10^{-5}$	$12/0.89 \times 10^{-5}$

3.2. Thermal model

The thermal model developed to determine the temperature field across the cell and the ceramic test system has been detailed by Laurencin et al. [41]. This model was coupled with the electrochemical model.

The thermal model takes into account heat transport by solid state conduction. Heat exchange between solid and gas by natural convection from the test bench to the furnace atmosphere and forced convection inside the gas channels were also taken into account.

Two kinds of radiation heat fluxes were assumed to occur. The first contribution corresponds to the heat exchanges between the ceramic test system and the furnace atmosphere. The second takes into account the heat exchanges between the free surface of the electrodes and the ceramic diffusers. Thermal source terms was also introduced, firstly because of heat generation due the endothermic and exothermic chemical reactions of the DIR process at the anode side and, secondly, because of thermal flow due to hydrogen anodic electro-oxidation.

The furnace temperature and the inlet gas temperature of the ceramic system correspond to the two boundary conditions of the geometry of the thermal model (cf. Fig. 2b). It was supposed that the fuel and air paths were sufficiently long to heat the gas to the furnace temperature (800 °C in this case).

The Reynolds number, *Re*, was calculated for all the gas channels of the system. In this configuration, the local Reynolds number remains much lower than 200 and indicates a laminar flow in the channels of the ceramic test system. The energy balance for the fuel and air channels was expressed by the following equation for a contact area *dS* between gas and solid:

$$\sum_i \frac{\partial(\dot{n}_i C_{p_i} T_g(r))}{\partial r} dr = h dS(T_s(r) - T_g(r)) \quad (8)$$

where n_i and C_{p_i} are the molar flow and the specific heat of each species *i*, *r* the channel flow axis, T_s the wall temperature of the solid and T_g the gas temperature. The heat exchange coefficients *h* were calculated (Eq. (9)) by using the Nusselt number, *Nu*, the hydraulic diameter of the channels, D_H and the heat conductivity of the gas mixture, λ [42].

$$h = \frac{Nu\lambda}{D_H} \text{ (W m}^{-2}\text{ K}^{-1}\text{)} \quad (9)$$

Nu tends to an asymptotic value depending on the channel configurations ($3.4 < Nu < 5.3$ [43,44]). For the heat exchange by

Table 2
Kinetic constants and electrochemical parameters of the electrochemical model [39,40].

Steam reforming reaction	$v_1 = k_1 P_{CH_4} P_{H_2O} - k_{-1} P_{CO} P_{H_2}^3$ (mol m^{-2} s^{-1})	$E_{a1} = 225$ kJ mol^{-1} $k_1^0 = 2.10^{13}$ mol bar^{-2} s^{-1} m^{-2}
CO_2 reforming reaction	$v_2 = k_2 P_{CH_4} P_{CO_2} - k_{-2} P_{CO}^2 P_{H_2}^2$ (mol m^{-2} s^{-1})	$E_{a2} = 225$ kJ mol^{-1} $k_2^0 = 2.10^{13}$ mol bar^{-2} s^{-1} m^{-2}
WGS reaction	$v_3 = k_3 P_{CO} P_{H_2O} - k_{-3} P_{CO_2} P_{H_2}$ (mol m^{-3} s^{-1})	$E_{a3} = 104$ kJ mol^{-1} $k_3^0 = 2.10^{8}$ mol bar^{-2} s^{-1} m^{-3}
Exchange current density	130 mA cm^{-2} [39]	
$i_{lim,\ cathode}$	10000 mA cm^{-2}	
Electrolyte conductivity (YSZ)	0.035 S cm^{-1} (T = 800 °C) [40]	

convection between the test system and the furnace atmosphere, the coefficient h was determined considering natural convection.

For the present configuration system, the governing equation for the temperature of solids was expressed in terms of conduction, convection, radiation and sources terms. Thus, the energy balance is given by equation 10 for a solid volume dV:

$$\lambda \nabla^2 T_s dV + d\dot{Q} = h dS(T_s - T_g) + d\phi \tag{10}$$

The first term, $\lambda \nabla^2 T_s dV$, is related to the heat transport in solid phase by conduction. The coefficient λ is the thermal conductivity of the materials. In the porous electrodes, only conduction was considered ($Pe \ll 1$, convection was neglected [45]). The effective thermal conductivity, λ_{eff} was calculated via the following mixture law:

$$\lambda_{eff} = \varepsilon\lambda_g + (1-\varepsilon)\lambda_s \,(\mathrm{W\ m^{-1}\ K^{-1}}) \tag{11}$$

where ε corresponds to the electrode porosity (g and s for gas and solid).

The second term of the energy balance equation (Eq. (10)), the source term $d\dot{Q}$, is the sum of two contributions. The first one is the thermal flow due to H_2 anodic electro-oxidation (Eq. (12)) and the second is the thermal flow related to the methane reforming process (Eq. (13)).

$$d\dot{Q}_1 = \left(-\Delta H_{H_2O}\frac{i}{2F} - U_{cell} i\right) dS \tag{12}$$

$$d\dot{Q}_2 = \left(\sum_{i=1}^{i=3} \nu_i \Delta H_i\right) dV \tag{13}$$

with ΔH_{H_2O} the hydrogen oxidation enthalpy, ν_i and ΔH_i respectively, the rates and the enthalpies of the chemical reactions (Eqs. (1)–(3)).

The radiation term of the energy balance equation (Eq. (10)), $d\phi$, is also the sum of two contributions. The first one corresponds to the heat exchange by surface-to-surface radiation between the anode (or cathode) and the adjacent flat ceramic plates (Fig. 2b), which is calculated using the general expression between two infinite parallel planes (Eq. (14)). The second contribution corresponds to the radiative loss from the test bench to the furnace atmosphere (Eq. (15)).

$$d\phi_1 = \frac{\sigma\varepsilon_{electrode}\varepsilon_{ceramic\ plate}}{1-(1-\varepsilon_{electrode})(1-\varepsilon_{ceramic\ plate})} (T^4_{electrode} - T^4_{ceramic\ plate}) dS \tag{14}$$

$$d\phi_2 = \varepsilon_{ceramic}\sigma(T_s^4 - T^4_{furnace}) dS \tag{15}$$

where ε_j is the medium emissivity (anode, cathode or ceramic plates), σ the Stefan–Boltzmann's constant and T_s the external surface temperature of the ceramic test system. Table 3 summarizes the different parameters of the thermal model.

3.3. Thermodynamic calculations

In the literature, numerous publications refer to the method of Gibbs energy minimization to determine the thermodynamic state where the carbon deposit is unstable and operate the cell in this domain [1,3,4,16,17,35]. The thermodynamic calculations were carried out by assimilating the stationary conditions to quasi-equilibrium conditions. A commercial code was used to determine the chemical equilibria which take place at different temperatures and pressures as a function of the chemical species present in the system.

Thermodynamic calculations were carried out with the "GEMINI" software (for Gibbs Energy MINImizer) [49], a thermodynamic

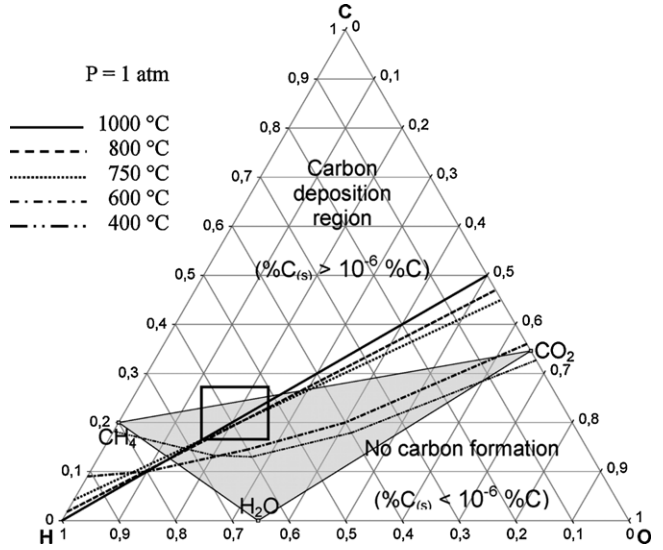

Fig. 3. Carbon deposition limits in a C—H—O ternary diagram calculated at different temperatures and under 1 atm [49].

code developed by the "Thermodata" association (INPG and CNRS collaboration, France). The database composed of C, H, O and Ar elements was created with the "COACH" software, which allows taking into account 141 chemical species ($C_nH_mO_x$, $n \leq 4$). The equilibrium state of the system was calculated using the following equation by introducing the molar quantities of C, H, O and Ar representative of the gas mixture studied at constant temperature and pressure:

$$(\Delta G_{system})_{T,P} = \left(\sum_{j=1}^{j} n_j \cdot \Delta G_j\right)_{T,P} = 0 \tag{16}$$

For a two-phase gas-solid equilibrium (case of high temperatures, $j=2$) and at constant pressure and temperature, the total Gibbs Energy is given by the following equation:

$$\Delta G_{system} = \sum_{i_g=0}^{i_g} n_{i_g}\left(\Delta G^0_{f,i_g} + RT\ln\left(\frac{n_{i_g}}{\sum_{i=1}^{i_g} n_{i_g}}\cdot P\right)\right) + \sum_{i_s=0}^{i_s} n_{i_s}\Delta G^0_{f,i_s} = 0 \tag{17}$$

$\Delta G^0_{f,i_g}$ and $\Delta G^0_{f,i_s}$ are, respectively, the Gibbs energy of formation of gaseous and solid species ($n_{i_g} = n_{CH_4}$, n_{CO_2}, n_{H_2O}, n_{CO}, n_{H_2} and $n_{i_s} = n_c$), expressed using the polynomial form $\Delta G^0_{f,i} = a + bT$. The composition of the system as a function of the initial molar composition of C, H, O and Ar was obtained by solving equation 17 with a minimization algorithm based on mass balance conservation.

Considering the initial molar gas composition (i.e. %C—H—O in the anodic fuel), it can be determined if carbon formation is significant by assuming equilibria to be achieved. Thanks to this method, the carbon deposition region can be delineated in a ternary diagram representative of the three active elements (C—H—O). The results of the calculation of the carbon deposition region boundaries are shown in Fig. 3 for various temperatures between 400 and 1000 °C at constant pressure (1 atm). The limits between the two regions correspond to a quantity of solid graphite equal to a millionth of the carbon initially present in the fuel.

The grey area in the C—H—O diagram corresponds to the humidified CH_4/CO_2 mixtures studied. The representative operating points

Table 3
Thermal parameters of cell and test facility materials [45–48].

	Anode	Electrolyte	Cathode	Ceramic (Al_2O_3)
λ ($W\,m^{-2}\,K^{-1}$)	3 (calculated)	3.8 [45]	1.8 (calculated)	10 [46]
ε	0.3 (estimated)	0.4 [47]	0.8 (estimated)	0.5 [48]

are localized in this area (partial pressures of gas species, i.e. %C—H—O, and the temperature in the anode calculated via the electrochemical and thermal models). The cell polarization can lead to an extension of the domain through the addition of O in the system according to Faraday's law:

$$N_{O_2} = \frac{i}{4F}\,(\text{mol s}^{-1}\,\text{m}^{-2}) \tag{18}$$

As a rule, in the domain studied, the risk of carbon deposition increases with decreasing temperature (within the grey area, the carbon deposition region extends with increasing temperature).

4. Results and discussion

4.1. Experimental results

4.1.1. Current–voltage measurements

Fig. 4 shows the electrochemical performances of the cell directly fed with humidified CH_4/CO_2 mixture. This polarization curve was obtained for the fuel composition D ($\dot{n}_{CH_4} = 25\,\text{mL min}^{-1}$, $x_{CH_4} = 0.12$) and compared to the performances obtained under humidified hydrogen ($\dot{n}_{CH_4} = 225\,\text{mL min}^{-1}$) for the same fuel utilization ($U_f = 30\%$ at $400\,\text{mA cm}^{-2}$). The fuel utilization, U_f, or faradic efficiency, was calculated according to the equation 19:

$$U_f = \frac{I}{nF\dot{n}_i}\,(\%) \tag{19}$$

U_f is the fraction of the fuel utilized electrochemically, with I the total current produced by the cell (A)n, the number of electrons (equal to 2 for the H_2 oxidation and 8 for the CH_4 oxidation in the case of biogas fuel cell) and $\dot{n}$ the molar flow of the anodic fuel (in mol s^{-1} in the Eq. (19)).

The OCV under humidified hydrogen was higher than the OCV under biogas ($E_{i=0} = 1.07\,V$ and $1.99\,V$ respectively for H_2/H_2O and $CH_4/CO_2/H_2O$ mixtures). The difference comes from the fact that the equilibrium oxygen partial pressure in the CH_4/CO_2 mixture is higher than that in the H_2/H_2O mixture. The Area Specific Resistances (ASR) were, however, found to be very similar ($ASR = 1.2\,\Omega\,\text{cm}^2$ and $1.3\,\Omega\,\text{cm}^2$, respectively, for H_2 and CH_4/CO_2 mixtures). The maximum power density under biogas matches the cell performance obtained under hydrogen (respectively $P = 207\,\text{mW cm}^{-2}$ and $245\,\text{mW cm}^{-2}$ for CH_4/CO_2 mixtures and H_2 with $U_f = 30\%$).

Fig. 5 shows the polarization curves plotted for the B, C, D, E and F fuel compositions. The U–I curves were recorded point-by-point by measuring, after ca. 1-min stabilization time, the electrode voltage as a function of the current passing through the anode. The effects of the methane mole fraction upon the electrochemical characteristics are summarized in Table 4. The electrochemical performance is improved when the CH_4 mole fraction increases. However, the maximum power density reaches a plateau when the methane feeding increases (up to $210\,\text{mW cm}^{-2}$ for $x_{CH_4} = 0.12$, 0.24 and 0.47). At the same time, the fuel utilization increases when the fuel flow rate is lowered ($U_f = 8\%$ and 93%, respectively, for $x_{CH_4} = 0.47$ and $x_{CH_4} = 0.03$) [50]. Therefore, a compromise needs to be found between a sufficient power density and acceptable fuel utilization.

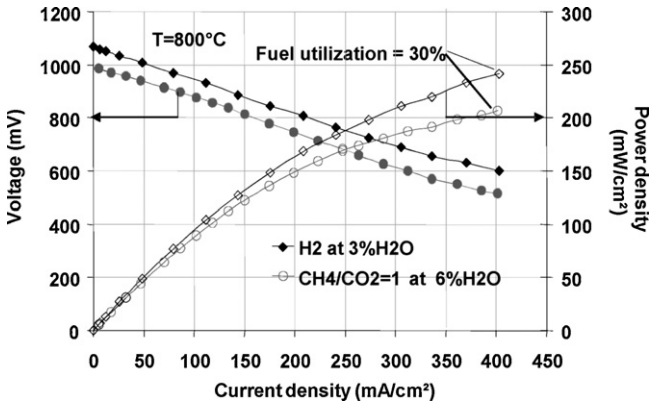

Fig. 4. Polarization curves at 800 °C under hydrogen (fuel composition A) and biogas (fuel composition D). Cell voltage and power density are plotted as a function of current density.

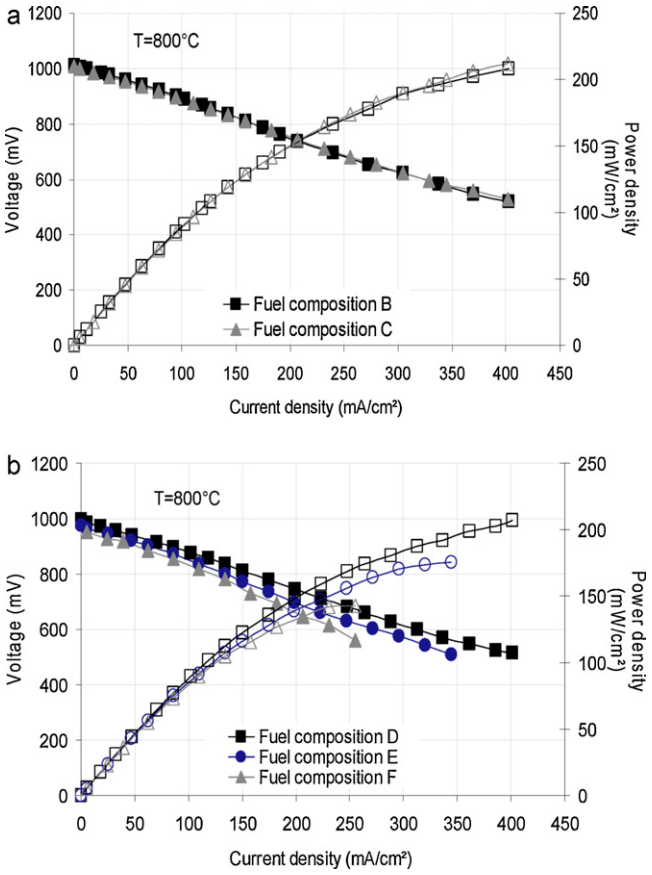

Fig. 5. Polarization curves at 800 °C under biogas for the B, C, D, E and F fuel compositions. The electrochemical characteristics are summarized in the table. (a) Polarization curves under biogas for the B and C fuel compositions: decreasing the methane flow rate has no effect on the power densities for low fuel utilization ($U_f \leq 16\%$). (b) Polarization curves under biogas for the D, E and F fuel compositions: the power densities decrease with decreasing methane flow rate for high fuel utilization ($U_f \geq 30\%$).

Table 4
Electrochemical properties determined at 800 °C under biogas.

Fuel composition (x_{CH_4})	CH_4 (mL min^{-1}/mol s^{-1})	OCV/E_{th} (V)	ASR (Ω cm^2) (at 0.7 V)	P_{max} (mW cm^{-2})	U_f (%) (at P_{max})
A ($x_{CH_4} = 0$)	0/0	1.07/1.1	1.2	245	30
B ($x_{CH_4} = 0.47$)	$100/7.45 \times 10^{-5}$	1.01/1	1.3	210	8
C ($x_{CH_4} = 0.24$)	$50/3.73 \times 10^{-5}$	1.01/0.98	1.3	210	16
D ($x_{CH_4} = 0.12$)	$25/1.86 \times 10^{-5}$	0.99/0.97	1.3	207	30
E ($x_{CH_4} = 0.06$)	$12/0.89 \times 10^{-5}$	0.97/0.96	1.5	175	53
F ($x_{CH_4} = 0.03$)	$6/0.45 \times 10^{-5}$	0.96/0.95	1.8	140	93

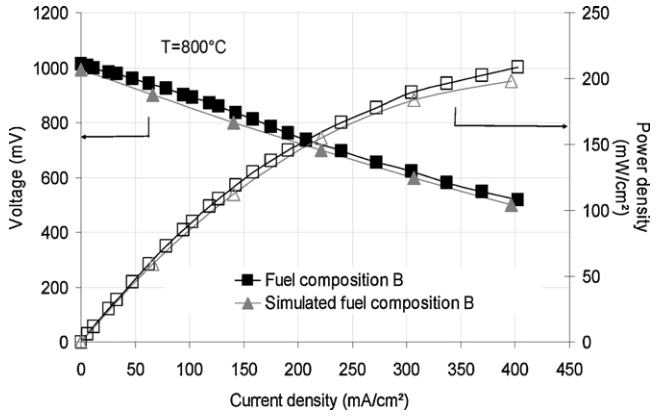

Fig. 6. Comparison between experimental and simulated polarization curves at 800 °C for the B fuel composition.

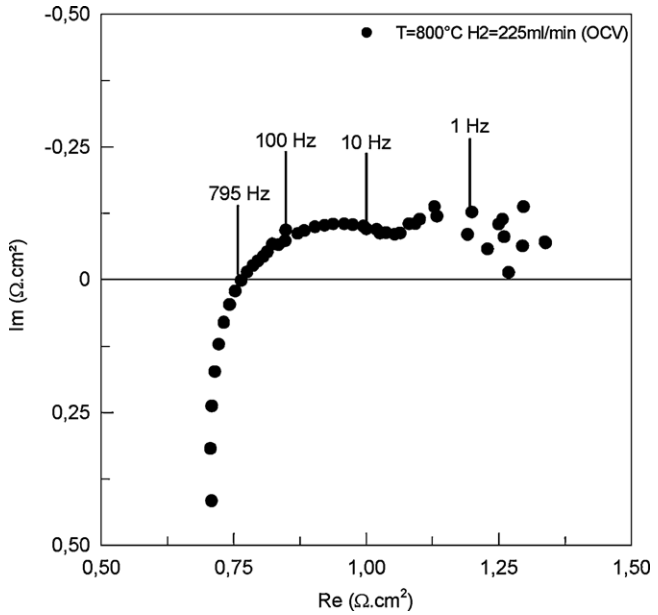

Fig. 7. Nyquist diagram of the cell under hydrogen (fuel composition A) at 800 °C and at the OCV.

4.2. Simulation results

4.2.1. Simulated current–voltage curves

Fig. 6 compares the simulated and experimental polarization curves obtained for the B fuel composition. Good agreement is observed between the simulated and experimental OCVs (1.07 V). The best fit between the two curves was obtained with a contact resistance between current collectors and electrodes, R_c, evaluated by impedance measurement, equal to 0.7 Ω cm^2 (cf. Fig. 7). This value represents about half the *ASR* value and is partly due to an insufficient compressive stress applied on the current collectors. For all fuel compositions tested, the simulated polarization curves are in agreement, with a good accuracy, with the experimental data with $R_c = 0.7\ \Omega\,cm^2$. These results tend to validate the choice of the input parameters of the electrochemical model, especially the methane reforming kinetic constants (cf. Table 2).

4.2.2. Simulated reaction rates and partial pressures

Thanks to the electrochemical model, reaction rates of WGS, CO_2 and H_2O reforming (respectively, Eqs. (3)–(1)) and partial pressures of the fuel components within the anode can be calculated as a function of the cell voltage and initial fuel composition. For the B fuel composition and at a cell voltage of 0.7 V, Figs. 8 and 9 give the illustration of these maps. The CO_2 reforming reaction rate (Fig. 8b) is much higher than the other reaction rates at the inlet of the cell (cell radius $r = 20$ mm; anode thickness $z = 1.5$ mm). The CO_2 reforming reaction is promoted because of the high CH_4 and CO_2 partial pressures (Fig. 9a and d) and of the high catalytic activity of Ni. The WGS reaction rate presents a sharp decrease at the inlet of the cell (Fig. 8a). Simultaneously, the Reverse WGS reaction (RWGS) is favoured. Indeed, the CO_2 concentration is still high and H_2 is mainly produced by the CO_2 reforming reaction. Moreover, CO and H_2O components are mainly produced by the RWGS reaction near the gas channel ($15 \le r \le 20$ mm and $z = 0$ mm). Close to the cell centre ($0 \le r \le 15$ mm and $z = 0$ mm), the RWGS reaction rate decreases because of the CO_2 reforming reaction simultaneously occurs along the cell (consumption of CO_2 via CO_2 reforming reaction, Fig. 8b). At the anode/electrolyte interface ($z = 1.5$ mm), the WGS reaction seems to be at equilibrium all over the cell. The reaction rate of the H_2O reforming (Fig. 8c) remains much lower than those of the other reactions and is mainly promoted at the inlet of gas fuel.

In our simulation study, the molar fraction distributions of gas species in the anode are mainly governed by the CO_2 reforming reaction (consumption of CO_2 and CH_4 species and production of H_2 and CO from the inlet to the outlet of the cell, Fig. 9a, d, b and e, respectively). As shown in Fig. 9c, a gradient of the H_2O species through the anode thickness was observed. Indeed, H_2O is mainly produced by the H_2 anodic electro-oxidation, which takes place at the anode/electrolyte interface ($z = 1.5$ mm). It should be noted that the CO production along the anode is important (Fig. 9e). Even if Ni-YSZ anodes do not catalyze the oxidation of CO [51], a small fraction of CO might be converted to CO_2 by anodic oxidation. The simulated electrochemical performance could be under-estimated (CO anodic oxidation was neglected in the present model).

4.2.3. Carbon formation study

SOFC operations strongly depends on the anodic fuel composition and cell voltage. In order to optimize the cell operation in terms of performance and durability in relation to carbon formation, simulated maps were plotted as functions of these two parameters, under biogas (CH_4/CO_2, ratio equal to 1, gas

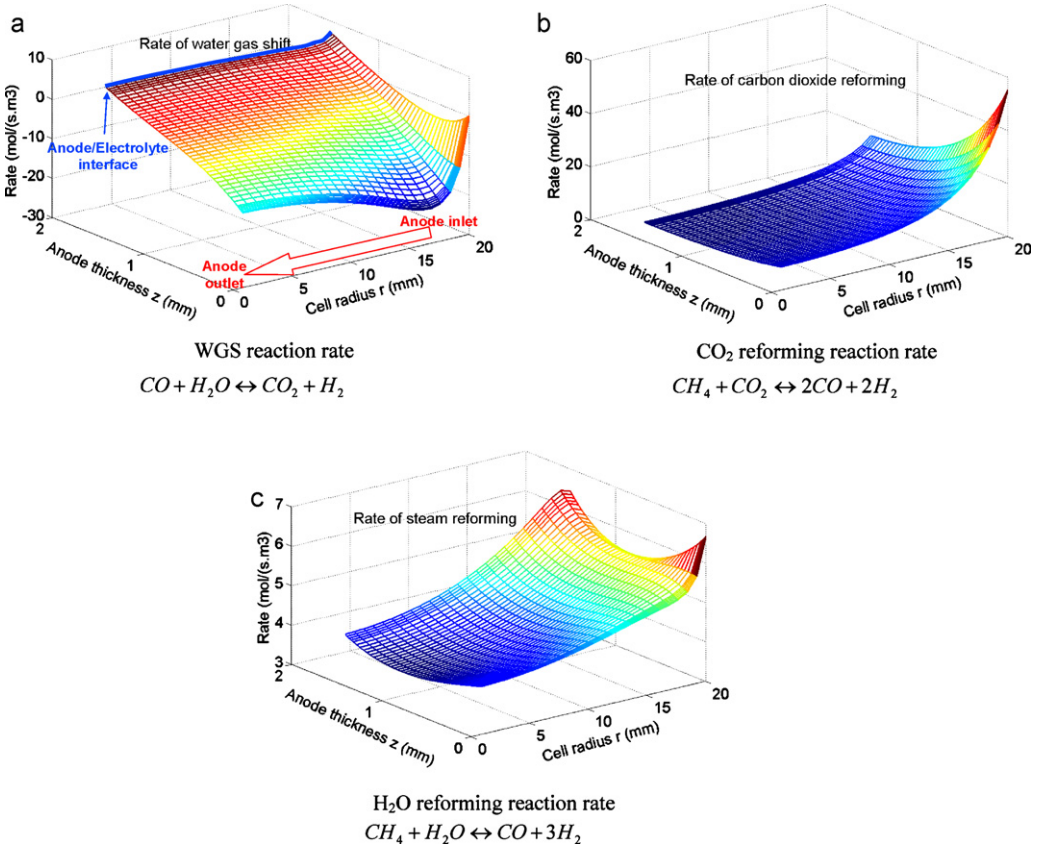

Fig. 8. Chemical reaction rates of WGS (a), CO_2 reforming (b) and H_2O reforming (c) at a cell voltage equal to 0.7 V for the B fuel composition at 800 °C plotted as functions of cell radius *r* and anode thickness *z*.

humidified at 6%). Fig. 10 gives the results of the map calculation of cell power density and cell temperature as functions of cell voltage ($0.5\,V \leq U_{cell} \leq OCV$) and CH_4 flow rate ($35 \leq \dot{n}_{CH_4} \leq 100\,ml\,min^{-1}$, $0.16 \leq x_{CH_4} \leq 0.47$)

Thermodynamic calculations were carried out to evaluate the risk of carbon deposition depending on U_{cell} and $\dot{n}_{CH_4}$. C—H—O ratio and cell temperature were determined for all the operating points using the electrochemical and thermal models. The calculations do not take into account the local repartition of the species within the cermet. The average values of the molar fractions of the chemical species within the whole anode were plotted in the diagram. All the points were located in a C—H—O ternary diagram in order to determine the thermodynamic risk of carbon formation. Fig. 11 shows the simulated points reported in a C—H—O diagram with the carbon deposition limiting lines calculated at 800, 775 and 750 °C (cf. Fig. 3).

Maximum power densities were obtained at high CH_4 flow rates and at high cell polarizations (Fig. 10a, $P \approx 180\,mA\,cm^{-2}$ for $\dot{n}_{CH_4} \approx 100\,mL\,min^{-1}$ and $U_{cell} \approx 0.6\,V$).

As can be seen in Fig. 10b, cell temperature varies from 730 °C ($\dot{n}_{CH_4} \approx 100\,mL\,min^{-1}$ and $U_{cell} \approx OCV$) to 810 °C ($\dot{n}_{CH_4} \approx 35\,mL\,min^{-1}$ and $U_{cell} \approx 0.5\,V$). Close to the OCV operation, the heat released by H_2 electro-oxidation is not sufficient to balance the endothermic heat fluxes due to CH_4 reforming reactions. Consequently, the cell temperature is lower than that of the furnace (fixed at 800 °C) and a heat flux is supplied by the furnace to heat the cell. On the contrary, at high cell polarizations, T_{cell} exceeds the furnace temperature. These operation conditions correspond to an exothermic cell operation. The autothermic conditions ($T_{cell} = T_f = 800\,°C$) were achieved for $\dot{n}_{CH_4} \approx 50\,mL\,min^{-1}$ and $U_{cell} \approx 0.6\,V$ which correspond to a cell power density $\approx 160\,mW\,cm^{-2}$.

The four CH_4 flow rates studied at different cell voltage were reported in a C—H—O diagram (cf. Fig. 11). Every point characterizing cell operation ($\dot{n}_{CH_4}$; U_{cell}) corresponds to a given cell temperature and C—H—O ratio (T_{cell}; %C—H—O). As a rule, the risk of carbon deposition decreases with decreasing CH_4 mole fractions in the fuel composition (low %C) and with decreasing cell voltage (high %O). Indeed, under polarization, oxygen species are carried from the cathode to the anode through the electrolyte and decrease the risk of carbon formation.

In Fig. 10, the black cross on the temperature map corresponds to ($\dot{n}_{CH_4} = 35\,ml\,min^{-1}$; $U_{cell} = 0.5\,V$). According to the cell temperature and the C—H—O ratio, i.e. $T_{cell} = 810\,°C$; %C—H—O = 23–50–27, this point is located below the limiting line at 800 °C where no carbon formation occurs. In the same way, the black triangle in the temperature map ($\dot{n}_{CH_4} = 50\,ml\,min^{-1}$; $U_{cell} = OCV$) corresponds to $T_{cell} = 770\,°C$; %C—H—O = 25–51–24 and is located in the region where the risk of carbon deposition exists.

A binary representation of the C—H—O diagrams can be used to determine the "safe" operating conditions as a function of CH_4 flow rate and cell voltage. These "safe" operating conditions correspond to the "0" values in the binary system represented in Fig. 12. In our operating conditions, at high CH_4 flow rate and at high cell voltage, the risk of carbon formation in the anode is important ("1" values in the binary system). On the opposite, carbon formation is avoided when $\dot{n}_{CH_4} < 60\,mL\,min^{-1}$ and $U_{cell} < 0.7\,V$. These conditions correspond to a threshold current density $\approx 200\,mA\,cm^{-2}$ to apply in order to maintain stable operation of the cell. These results were confirmed experimentally, and will be the subject of

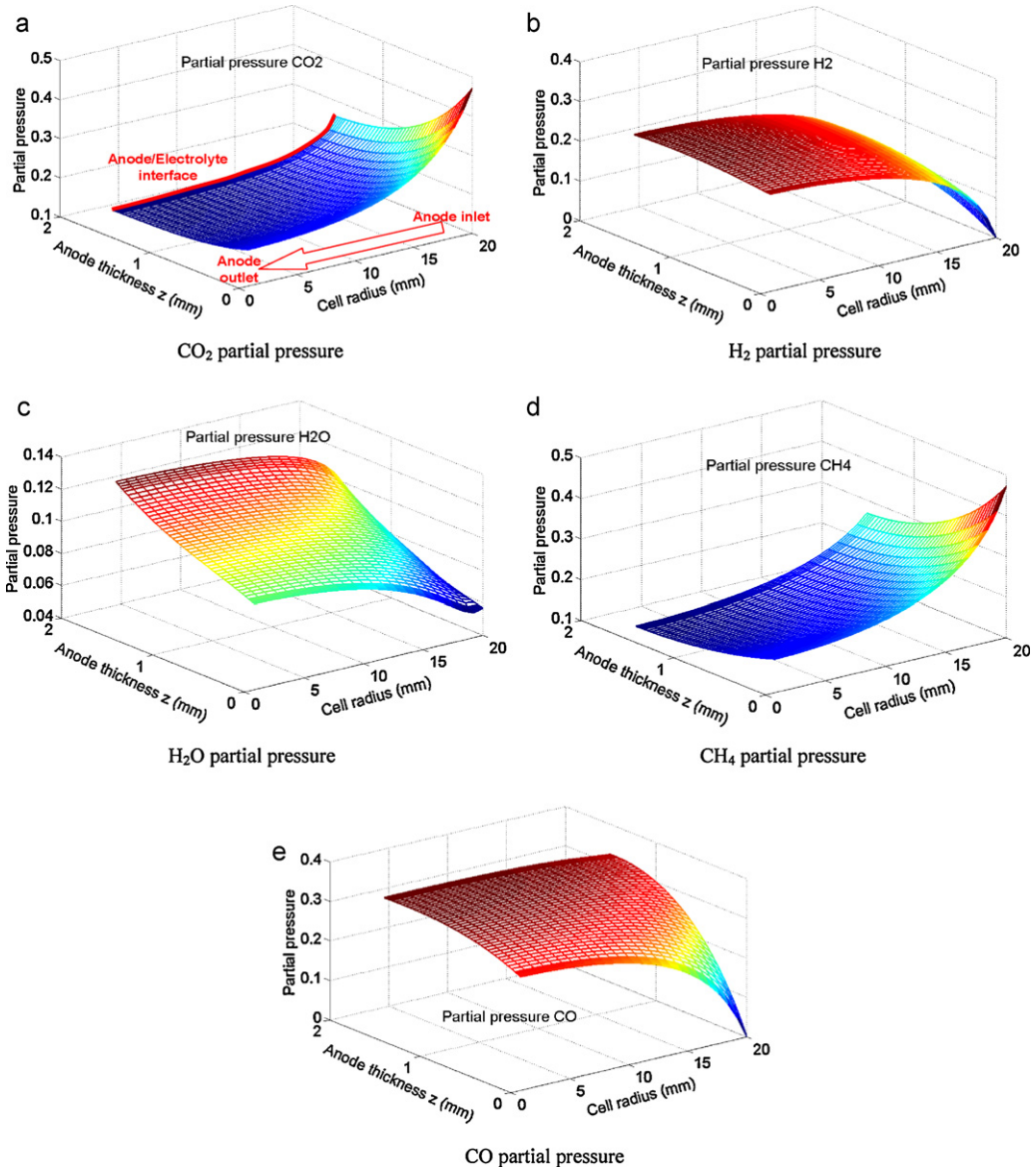

Fig. 9. Partial pressures of the fuel components at a cell voltage equal to 0.7 V and for the B fuel composition at 800 °C: (a) CO_2 partial pressure, (b) H_2 partial pressure, (c) H_2O partial pressure, (d) CH_4 partial pressure and (e) CO partial pressure. These pressures are plotted as functions of cell radius *r* and anode thickness *z*.

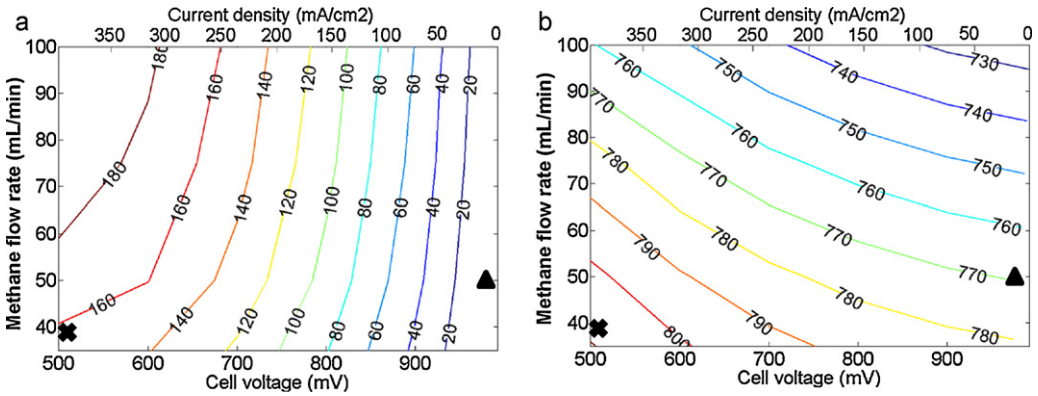

Fig. 10. Calculated map of the cell power density (a) and of the cell temperature (b) plotted as functions of cell voltage and CH_4 flow rate (CH_4/CO_2 ratio equal to 1, gas humidified at 6%).

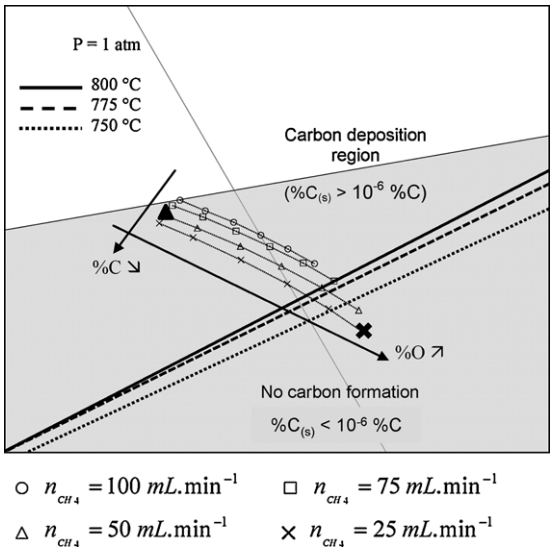

Fig. 11. Carbon deposition limiting lines in a C—H—O diagram at 800, 775 and 700 °C and at 1 atm. Localization of operating points obtained at different CH_4 flow rates (%C decreases with decreasing the CH_4 concentration in the fuel) and cell voltage (%O increases with the cell polarization) (the domain studied is represented by a square plotted in Fig. 3).

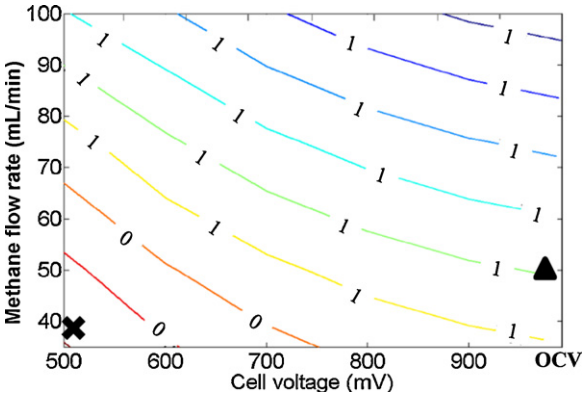

Fig. 12. Calculated map of the risk of carbon deposition plotted as a function of cell voltage and CH_4 flow rate (CH_4/CO_2 ratio equal to 1, gas humidified at 6%). Operation in the carbon free region is represented by "0" values in the binary representation system.

another paper under progress. Preliminary results have been published [52].

5. Conclusion

In this work, internal reforming over Ni-YSZ cermet anode in SOFC operating under biogas was investigated. Experimental study of a standard SOFC with synthetic simulated biogas (CH_4/CO_2 ratio equal to 1, gas with 6% humidity) shows good electrochemical performances at 800 °C (for $U_f = 30\%$, $P \approx 210\ mW\ cm^{-2}$ under biogas in comparison to $P \approx 240\ mW\ cm^{-2}$ under humidified hydrogen). This result tends to validate the direct biogas reforming as a suitable way to produce electrical power in a SOFC.

In parallel to the experiments, thermodynamic calculations and modelling were carried out to evaluate the risk of carbon deposition depending on CH_4 concentration in the fuel gas and on cell voltage. A CH_4 flow rate of ~60 mL min^{-1} and a cell voltage of ~0.6 V are required to limit the carbon deposition and to preserve autothermic cell operation. In the conditions of our study (with a contact resistance of 0.7 $\Omega\ cm^2$), these operating parameters correspond to a power density around ~160 $mW\ cm^{-2}$.

However, the confrontation between experimental and modelling results has to be completed. Indeed, C—H—O diagram and model results were employed here to predict the risk of carbon formation for DIR-SOFCs from a thermodynamical point of view. The thermodynamic calculations are useful to adjust initial fuel compositions or cell voltage in order to limit carbon formation. The durability of the cell operated in biogas internal reforming was studied over 400 h. Preliminary results have been published [52].

Acknowledgements

The authors acknowledge Dr M. Petitjean and Dr. B. Morel for their assistance.

References

[1] K. Eguchi, H. Kojo, T. Takeguchi, R. Kikuchi, K. Sasaki, Solid State Ionics 152 (2002) 411–416.
[2] J. Liu, S.A. Barnett, Solid State Ionics 158 (2003) 11–16.
[3] K. Sasaki, K. Watanabe, Y. Teraoka, J. Electrochem. Soc. 151 (2004) A965–A970.
[4] K. Sasaki, M. Uchimura, K. Shiosaki, K. Susuki, K. Watanabe, H. Kusaba, Y. Teraoka, Proceedings of the European Solid Oxide Fuel Cell Forum, 2004, pp. 1534–1543.
[5] S. Park, J.M. Vohs, R.J. Gorte, Nature 404 (2000) 265–267.
[6] B. Huang, S.R. Wang, R.Z. Liu, T.L. Wen, J. Power Sources 167 (2007) 288–294.
[7] K. Yamaji, H. Kishimoto, Y. Xiong, T. Horita, N. Sakai, M.E. Brito, H. Yokokawa, J. Power Sources 159 (2006) 885–890.
[8] H. Kim, S. Park, J.M. Vohs, R.J. Gorte, J. Electrochem. Soc. 148 (2001) A693–A695.
[9] J.M. Klein, M. Hénault, C. Roux, Y. Bultel, S. Georges, J. Power Sources 193 (2009) 331–337.
[10] S. Park, R.J. Gorte, J.M. Vohs, J. Electrochem. Soc. 148 (2001) A443–A447.
[11] B. Huang, X.F. Ye, S.R. Wang, H.W. Nie, J. Shi, Q. Hu, J.Q. Qian, X.F. Sun, T.L. Wen, J. Power Sources 162 (2006) 1172–1181.
[12] H. Kim, C. Lu, W.L. Worrell, J.M. Vohs, R.J. Gorte, J. Electrochem. Soc. 149 (2002) A247–A250.
[13] O.A. Marina, C. Bagger, S. Primdahl, M. Mogensen, Solid State Ionics 123 (1999) 199–208.
[14] E. Perry Murray, T. Tsai, S.A. Barnett, Nature 400 (1999) 649–651.
[15] A. Weber, B. Sauer, A.C. Muller, D. Herbstritt, E. Ivers-Tiffee, Solid State Ionics 152 (2002) 543–550.
[16] Z. Zhan, Y. Lin, M. Pillai, I. Kim, S.A. Barnett, J. Power Sources 161 (2006) 460–465.
[17] J.H. Koh, Y.S. Yoo, J.W. Park, H.C. Lim, Solid State Ionics 149 (2002) 157–166.
[18] Y. Lin, Z. Zhan, J. Liu, S.A. Barnett, Solid State Ionics 176 (2005) 1827–1835.
[19] G. Goula, V. Kiousis, L. Nalbandian, I.V. Yentekakis, Solid State Ionics 177 (2006) 2119–2123.
[20] J. Staniforth, K. Kendall, J. Power Sources 71 (1998) 275–277.
[21] Z. Gao, K. Sekizawa, K. Eguchi, Electrochemistry 67 (1999) 336–339.
[22] D.J. Moon, J.W. Ryu, Catal. Today 87 (2003) 255–264.
[23] J. Huang, R.J. Crookes, Fuel 77 (1998) 1793–1801.
[24] C.M. Finnerty, N.J. Coe, R.H. Cunningham, R.M. Ormerod, Catal. Today 46 (1998) 137–145.
[25] R.J. Gorte, H. Kim, J.M. Vohs, J. Power Sources 106 (2002) 10–15.
[26] R.J. Gorte, J.M. Vohs, J. Catal. 216 (2003) 477–486.
[27] T. Takeguchi, R. Kikuchi, T. Yano, K. Eguchi, K. Murata, Catal. Today 84 (2003) 217–222.
[28] H. Sumi, K. Ukai, Y. Mizutani, H. Mori, C.J. Wen, H. Takahashi, O. Yamamoto, Solid State Ionics 174 (2004) 151–156.
[29] K. Kendall, C.M. Finnerty, G. Saunders, J.T. Chung, J. Power Sources 106 (2002) 323–327.
[30] G.J. Saunders, J. Preece, K. Kendall, J. Power Sources 131 (2004) 23–26.
[31] A. Abudula, M. Ihara, H. Komiyama, K. Yamada, Solid State Ionics 86 (1996) 1203–1209.
[32] T.J. Huang, M.C. Huang, J. Power Sources 168 (2007) 229–235.
[33] Y. Lin, Z. Zha, S.A. Barnett, J. Power Sources 158 (2006) 1313–1316.
[34] V. Alzate-Restrepo, J.M. Hill, Appl. Catal. A 342 (2008) 49–55.
[35] T. Takeguchi, Y. Kani, T. Yano, R. Kikuchi, K. Eguchi, K. Tsujimoto, Y. Uchida, A. Ueno, K. Omoshiki, M. Aizawa, J. Power Sources 112 (2002) 588–595.
[36] B. Morel, J. Laurencin, Y. Bultel, F. Lefebvre-Joud, J. Electrochem. Soc. 152 (2005) A1382–A1389.
[37] W. Lehnert, J. Meusinger, F. Thom, J. Power Sources 87 (2000) 57–63.
[38] J. Wei, E. Iglesia, J. Catal. 224 (2004) 370–383.
[39] J.W. Kim, A.V. Virkar, K.Z. Fung, K. Mehta, S.C. Singhal, J. Electrochem. Soc. 146 (1999) 69–78.
[40] S.C. Singhal, K. Kendall, High Temperature Solid Oxide Fuel Cell: Fundamentals, Design and Applications, Elsevier Ltd, 2003.
[41] J. Laurencin, F. Lefebvre-Joud, G. Delette, J. Power Sources 177 (2008) 355–368.
[42] J.F. Sacadura, Initiation aux transferts thermiques, Tec & Doc Lavoisier, 2000.
[43] B. Eyglunent, Manuel de thermique, théorie et pratique, Hermes Sciences Publications, 2000.

[44] Y.P Chyou, T.D. Chung, J.S. Chen, R.F. Shie, J. Power Sources 139 (2005) 126–140.
[45] T. Ackmann, L.G.J. De Haart, W. Lehnert, D. Stolten, J. Electrochem. Soc. 150 (2003) A783–A789.
[46] A.H. Heuer, L.W. Hobbs, Science and Technology of Zirconia, vol. 5, 1997.
[47] C.L. Yaws, Handbook of Thermal Conductivity, vol. 4, 1997.
[48] Y.S. Touloukian, D.P. De Witt, Thermal Radiative Properties, vol. 7–8, 1972.
[49] Thermodynamic properties of inorganic substances, http://thermodata.online.fr.
[50] T. Suzuki, S. Sugihara, K. Hamamoto, T. Yamaguchi, Y. Fujishiro, J. Power Sources 196 (2011) 5485–5489.
[51] O. Costa-Nunes, R.J. Gorte, J.M. Vohs, J. Power Sources 141 (2005) 241–249.
[52] K. Girona, J. Laurencin, M. Petitjean, J. Fouletier, F. Lefebvre-Joud, ECS Trans. 25 (2) (2009) 1041.

Nomenclature

C_p	specific heat ($J\,mol^{-1}\,K^{-1}$)
D_H	hydraulic diameter (m)
E_a	activation Energy ($kJ\,mol^{-1}$)
$E_{i=0}$	open circuit voltage (V)
F	Faraday constant ($96485\,C\,mol^{-1}$)
h	heat exchange coefficient ($W\,m^{-2}\,K^{-1}$)
i	current density ($A\,m^{-2}$)
k^0	orientation factor ($mol\,bar^{-2}\,s^{-1}\,m^{-2}$ or $mol\,bar^{-2}\,s^{-1}\,m^{-3}$)
k	kinetic constant ($mol\,bar^{-2}\,s^{-1}\,m^{-2}$ or $mol\,bar^{-2}\,s^{-1}\,m^{-3}$)
$\dot{n}$	molar flow ($mol\,s^{-1}$)
N	molar flux density ($mol\,s^{-1}\,m^{-2}$)
Nu	Nusselt number
Pe	Peclet number
P	partial pressure (Pa)
$\dot{Q}$	thermal source terms ($J\,s^{-1}$)
R	gas constant
Re	Reynolds number
R_t	electrolyte and contact resistances ($\Omega\,m^2$)
r	channel flow axis (m)
S	surface (m^2)
T	temperature (K)
T_g	gas temperature (K)
T_s	temperature of the solid (K)
U_{cell}	cell voltage (V)
U_f	fuel utilization (%)
V	volume (m^3)
v	chemical reaction rate ($mol\,s^{-1}\,m^{-2}$ or $mol\,s^{-1}\,m^{-3}$)
ε	porosity
ε_j	emissivity (j = LSM, YSZ, Ni-YSZ, Al_2O_3)
ϕ	radiative flux ($J\,s^{-1}$)
ΔH	enthalpy ($J\,mol^{-1}$)
ΔG	total Gibbs free energy ($J\,mol^{-1}$)
ΔG_0	standard Gibbs free energy ($J\,mol^{-1}$)
η_{act}	activation polarization (V)
η_{conc}	concentration polarization (V)
λ	thermal conductivity ($W\,m^{-1}\,K^{-1}$)
σ	Stefan Boltzmann's constant ($W\,m^{-2}\,K^{-4}$)